A Kinematic Description of the Key Flow Characteristics in an Array of Finite-Height Rotating Cylinders

Anna E. Craig
Department of Mechanical Engineering,
Stanford University,
Stanford, CA 94035
e-mail: craig0a@stanford.edu

John O. Dabiri
Professor
Department of Civil and
Environmental Engineering;
Department of Mechanical Engineering,
Stanford University,
Stanford, CA 94035

Jeffrey R. Koseff
Professor
Department of Civil and
Environmental Engineering,
Stanford University,
Stanford, CA 94035

Experimental data are presented for large arrays of rotating, finite-height cylinders to study the dependence of the three-dimensional (3D) mean flows on the geometric and rotational configurations of the array. Two geometric configurations, each with two rotational configurations, were examined at a nominal Reynolds number of 600 and nominal tip-speed ratios of 0, 2, and 4. It was found that the rotation of the cylinders drives the formation of streamwise and transverse flow patterns between cylinders and that net time–space averaged transverse and vertical flows exist within the developed flow region of the array. This net vertical mean flow provides an additional mechanism for the exchange of momentum between the flow within the array and the flow above it, independent from the turbulent exchange mechanisms which are also observed to increase by almost a factor of three in a rotating array. As an array of rotating cylinders may provide insight into the flow kinematics of an array of vertical axis wind turbines (VAWTs), this planform momentum flux (both mean and turbulent) is of particular interest, as it has the potential to increase the energy resource available to turbines far downstream of the leading edge of the array. In the present study, the streamwise momentum flux into the array could be increased for the rotating-element arrays by up to a factor of 5.7 compared to the stationary-element arrays, while the streamwise flow frontally averaged over the elements could be increased by up to a factor of four in the rotating-element arrays compared to stationary-element arrays. [DOI: 10.1115/1.4032600]

1 Introduction

Developing from literature concerning the wake dynamics and instabilities associated with a single rotating cylinder (see, e.g., Refs. [1,2]), in recent years the dynamics of paired rotating cylinders have also become of interest (see, e.g., Refs. [3–8]). It has been shown that for specific regimes of geometric configuration, rotational configuration, Reynolds number, and rotation rate, suppression of bluff-body vortex shedding is observed. A table of the parameter ranges previously studied is compiled in the Supplemental material which is available under the "Supplemental Material" tab on the ASME Digital Collection. Of particular note is the combined experimental and numerical study by Chan et al. [3], which reported not only the existence of vortex suppression regimes but also generally increasing lift coefficients and decreasing drag coefficients with increasing cylinder rotation rate.

Extending these two-cylinder studies, the present study examines the interactions of many rotating cylinders in an array. Experiments on an array of almost 300 rotating elements were conducted in order to determine the horizontal flow interactions between rotating cylinders as a function of geometric configuration, rotational configuration, and rotation rate. The two orders of magnitude increase in the number of rotating cylinders considered was motivated by the potential practical implications of the study. In recent years, arrays of VAWTs have been proposed as a distinct approach to wind energy. Instead of large, individually efficient horizontal axis wind turbines (HAWTs) sparsely spread over a large land area, VAWTs are small, often individually less efficient, but able to be densely arranged with the potential for beneficial interaction between neighboring turbines (see, e.g., Refs. [9,10]).

Experimental field measurements made by Dabiri [9] indicated a significant increase in the power output of a counter-rotating pair of VAWTs in comparison with the power output of the turbines operating in isolation. (These results were examined by analogy with the vortex suppression of paired rotating cylinders observed by Chan et al. [3].) Later, Ref. [11] numerically showed that a pair of rotating VAWT cross sections exhibit wake suppression behavior similar to that observed by Chan et al. [3] for a pair of rotating cylinder cross sections. The study by Duraisamy and Lakshminarayan [11] also began looking at the interaction between larger numbers of turbine cross sections, arranged in up to five infinite-extent rows. The interactions between turbines were observed to create regions of high momentum and also shifted regions of low-momentum wake deficits. As a result, depending on the array configuration, a given turbine in an array could have up to three times the power output of an isolated turbine or could have a zero power output.

The interaction of many turbines was also examined by Kinzel et al. [12] in a field array of 18 VAWTs arranged as nine pairs. Of particular importance was the observed interaction of the array with the flow immediately above it such that a significant turbulence-driven energy flux was observed vertically through the top of the array (termed the planform energy flux). Studies of HAWT arrays by Cal et al. [13] and Calaf et al. [14] have shown that the turbulence- and dispersive-driven planform energy fluxes are the primary energy sources for a turbine located deep in the interior of a large array. It is worthwhile to explicitly state that this indicates the mean horizontal energy flux into the frontal area of the array was depleted by the most upwind turbines and did not provide significant energy to the developed flow region. Furthermore, the developed flow region was determined to be horizontally homogeneous (that is, no time-–space averaged transverse or vertical flows) and thus no significant energy flux was provided to the arrays in the developed flow region by the mean flows either vertically or transversely.

Motivated by the important role vertical flows play in the dynamics of wind turbine arrays, the present work deviates from the prior rotating-cylinder studies of Ref. [3] and others: instead of modeling the system as quasi-two-dimensional (2D), a finite-height array was chosen. The present experiment thus allowed a

study of the 3D interactions between horizontal flow patterns such as observed by Chan et al. [3] and vertical flows such as observed by Cal et al. [13], Calaf et al. [14], and Kinzel et al. [12].

Finally, while the study by Calaf et al. [14] specifically focused on the developed flow dynamics deep in an array of HAWTs, the development of flow through an aerodynamically large array of either rotating cylinders or VAWTs remains largely unexplored. The present study, therefore, also seeks to provide a first step in understanding the development of flow through a rotating-element array, in particular if any developed flow region may be said to exist.

At this point, it is emphasized that while certain aspects of this study have been motivated by the potential implications for VAWT arrays, the designed experiment was not intended to provide results directly analogous to a physical VAWT array. Rather, the intention of the present work is to provide insight into the key flow characteristics in an array of rotating elements on which the future work may build. A complete discussion of the comparability between the present experimental work and a physical VAWT array is provided in the Supplemental material which is available under the "Supplemental Material" tab on the ASME Digital Collection.

The remainder of this paper is organized as follows: Section 2 briefly describes the experimental methods, including the notation, the experimental setup, the experimental parameters, and the presented uncertainties. Section 3 presents data and analysis relating to: (1) the determination of developed flow regions in the arrays, (2) the construction of mean 3D flow patterns within each array, (3) the determination of turbulence structure and organization within each array, (4) the comparison of streamwise momentum transport mechanisms for each array, and (5) the quantitative comparison of the different arrays. Section 4 discusses the implications which may be drawn from the presented data, particularly with respect to characteristics considered desirable for a VAWT array. Section 5 summarizes the findings and suggests avenues for future work.

2 Experimental Methods

2.1 Notation. Following the notation of Ref. [3], the gap, g, is defined to be the distance between the near edges of the cylinders. The nondimensional rotation rate is defined to be $\alpha = D\Omega/2u_0$, where D is the cylinder diameter, Ω is the rotational speed of the cylinder, and u_0 is the freestream velocity. Note that the definition of α must be interpreted in the context of an array with some care, as it is expected (e.g., Refs. [15–18]) that the local mean streamwise velocities within the array will be lower than freestream. Thus, the α as defined based on the freestream may be lower than a nondimensional rotation rate defined based on the local streamwise velocity for the same element rotation rate. The pertinent Reynolds number is defined by the cylinder diameter and freestream velocity, that is, $\mathrm{Re} = u_0 D/\nu$, where ν is the kinematic viscosity of the working fluid. The rotational configuration of a pair of cylinders is defined to be the doublet when the inner (adjacent) edges of the cylinders rotate in the upstream direction and the reverse-doublet when the inner edges rotate in the downstream direction.

Adopting the notation of Ref. [19], throughout this paper an over line will indicate a temporally averaged quantity and a prime will denote the deviation from the temporally averaged quantity (that is, $\theta = \overline{\theta} + \theta'$, where θ denotes a general flow variable). Brackets will denote the horizontal spatial average of a quantity and a tilde will denote the deviation from the horizontal spatial averaged quantity (that is, $\theta = \langle \theta \rangle + \tilde{\theta}$). The sequential time–space decomposition of a variable is then written as $\theta = \langle \overline{\theta} \rangle + \tilde{\overline{\theta}} + \theta'$. Extending the notation slightly to accommodate the experiments performed, if the horizontal average is taken over a sufficiently large region in streamwise direction, but with no averaging in the transverse direction, such a partial-spatial average will be denoted by a "ket," $|\theta\rangle$.

2.2 Experimental Setup. The following is an abbreviated description of the experimental setup. For full details, see the Supplemental material which is available under the "Supplemental Material" tab on the ASME Digital Collection.

The flow in a large array of cylinders was investigated experimentally in the recirculating water flume of Stanford University's Bob and Norma Street Environmental Fluid Mechanics Laboratory (EFML). Throughout this work, the coordinate system will be such that the positive x-axis is aligned with the freestream flow, the positive z-axis is vertically upward, and the y-axis is transverse across the flume width.

The arrays examined consisted of 532 or 560 circular cylindrical elements 12.7 mm in diameter (D) and 101.6 mm in height (H). All lengths in this work are normalized by the element diameter. As the aspect ratio of the cylinders had no precedent in the quasi-2D rotating cylinder work by Chan et al. [3] and others, the selected ratio was chosen to be in keeping with prior work on VAWT arrays by Dabiri [9] and Kinzel et al. [12].

Of these elements, the central 295 or 296 cylinders in a streamwise strip down the array were externally rotated by motors mounted above the flume via drive shafts extending through the water column. The remaining 265 or 226 elements were stationary "buffer" regions to each side of the central rotating strip. The rotation mechanism was composed of an array of spur gears with vertically oriented shafts that were sandwiched between an upper and lower plate. Some of the gear shafts were threaded and protruded through the top plate so that the cylindrical elements could be screwed on such that the cylinders were above the top plate (see Fig. 1(a)). The clearance of the cylinder above the top plate was approximately 1–2 mm, but this was not strictly enforced. The effects of this clearance space on the fluid flow were not evaluated. Elevated flat plates were placed in front of, behind, and to the sides of the gear assembly such that an offset bottom was created at the level of the top plate of the gear assembly throughout the test section (Fig. 1(b)). The farthest upstream plate in the flume was angled so as to provide a ramp up to the offset bottom. The lip of the plate served as a trip point for the boundary layer. The free surface was 43 cm above the top plate (bottom of the cylinders). As this was approximately four times the height of the array, the effects of the free surface were considered negligible.

The array was rotationally and geometrically reconfigurable. In the data presented here, two geometric configurations—staggered and paired—are considered, each with two rotational variations. These arrays will be referred to hereafter as the staggered RI, the staggered RII, the (paired) doublet, and the (paired) reverse doublet. Planform views of the spatial and rotational configurations are included in Fig. 2.

Two-dimensional particle image velocimetry (PIV) was used to capture the fluid motion in both horizontal (x–y) and vertical (x–z) planes, with a typical resolution of 2.5 mm (0.2D). In the horizontal sheet data, shadowing from the elements closer to the laser head prevented collection of PIV data between elements. Similarly, in the vertical sheet data, the camera could not image through elements and therefore no data was collected between elements along the rows. There was also a small but noticeable fore-shortening effect, in that the elements closest to the camera appeared taller than the elements farther away, and thus flow immediately above the distant elements could not be imaged.

2.3 Experiment Parameters. The mean freestream velocity and corresponding Reynolds number and α for the each array were as given in Table 1. All velocity data were normalized by the mean free-stream velocity. For convenience, the data will be referred to by the nominal Reynolds number and α, however, the actual values achieved varied from the nominal values as the result of discrete rather than continuous control over the initial setting of the flume flow speed (via raising/lowering the weir, increasing the pump frequency, etc.). Although differing from nominal values, once the conditions had been set for the experiment, the resulting flow speed was consistent over the course of the experiment.

For all four arrays, the measurements taken included one vertical sheet along the centerline of the array and one horizontal sheet
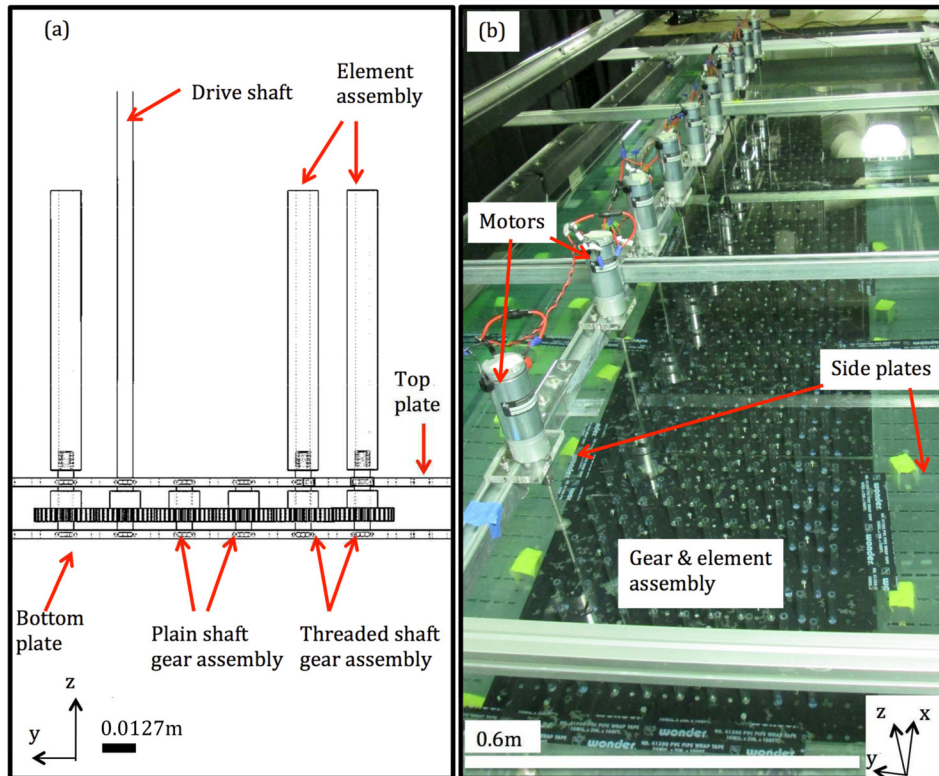
Fig. 1 Experimental setup illustrations. (*a*) Close-up sketch showing element mounting to gears and plate structure holding gears in place. (*b*) Photo of full array in the flume.
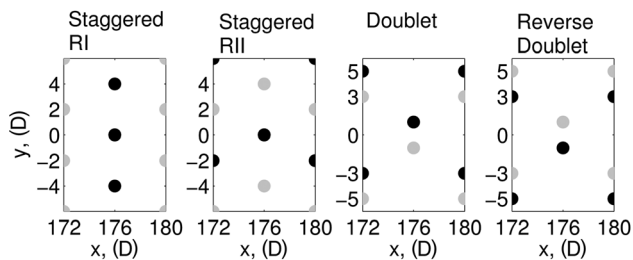

Fig. 2 Schematic showing planform views of array configurations. Black circles indicate clockwise rotating elements, gray circles indicate counterclockwise rotating elements, as viewed from above.

Table 1 Nominal and actual Reynolds numbers and α and corresponding measured free-stream velocities for the arrays

u_0 (m/s)	Re (nom.)	Re (act.)	α (nom.)	α (act.)
Staggered RI				
0.04688 ± 0.0002	600	595.6 ± 2.5	0	0
			1	0.99 ± 0.15
			2	2.00 ± 0.17
			4	4.00 ± 0.22
Staggered RII, paired doublet, paired reverse doublet				
0.04469 ± 0.0002	600	567.7 ± 2.5	0	0
			2	2.10 ± 0.18
			4	4.20 ± 0.24

at the midheight of the array at five locations along the length of the array: row 1 (0*D* downstream from leading edge), row 15 (56*D*), row 31 (120*D*), row 45 (176*D*), and row 59 (232*D*).

At the fourth measurement location (row 45, 176*D* downstream of the leading edge), additional vertical data sheets were taken in a transverse sequence and additional horizontal sheets were taken in a vertical sequence. For the staggered RI array, five vertical sheets were taken at distances of $-1D$, $-0.5D$, $0D$, $0.5D$, and $1D$ from the array centerline and four horizontal sheets were taken at 1.5*D*, 4.0*D*, 7.2*D*, and 8.7*D* above the bottom. For the staggered RII, paired doublet, and paired reverse doublet arrays, eight vertical sheets were taken at distances of $-3.0D$, $-2.0D$, $-1.0D$, $0D$, 1.0*D*, 2.0*D*, 3.0*D*, and 4.0*D* from the centerline and six horizontal sheets were taken at 2.0*D*, 6.0*D*, 4.0*D*, 7.5*D*, 8.5*D*, and 10.0*D* above the bottom. For a schematic of the measurement position in the arrays, please see the Supplemental material which is available under the "Supplemental Material" tab on the ASME Digital Collection.

At each measurement location 512 image pairs were taken at 0.75 Hz for the staggered RI array and 0.5 Hz for the other three arrays. Additionally, at the centerline and midheight data sheets at the fourth measurement position, additional sets of 512 image pairs were taken a 15 Hz for the staggered RI array and at 6 Hz and 15 Hz for the other three arrays. The lowest data sampling rates allowed each image pair to be statistically uncorrelated from the other image pairs. The higher data sampling rates allowed a more complete construction of the temporal turbulent power spectra and showed that no flow periodicities existed which would be expected to effect the interpretation of the lower sampling rate data.

2.4 Measurement Uncertainty. Explicitly quantifiable uncertainties associated with camera calibration, absolute positioning of the laser sheets within the array, statistical variations, and global alignment of the collected data were propagated through the analysis of the averaged velocity measurements. A thorough discussion of uncertainties is provided in the Supplemental material which is available under the "Supplemental Material" tab on the ASME Digital Collection, but typical ranges for these uncertainties are summarized in Table 2. Within these explicitly quantified uncertainties, data sets which would be expected to agree (the $\alpha = 0$ measurements for arrays of like geometry) were not

Source	Time–space averaged (u_0)	Time–space-depth averaged (u_0)
Camera calibration	0.004	0.004
Laser sheet, alignment with array	0.005–0.03	—
Statistical variations	0.001–0.005	0.0001–0.001
Global data alignment	—	0.0001–0.004
Unquantified variations	0.01–0.05	0.001–0.003

Uncertainties in the vertical velocities were usually on the lower ends of the ranges while uncertainties in the streamwise velocities were usually on the higher ends of the ranges.

within the range of uncertainties. This indicated that the experimental variations not explicitly quantifiable were significant. In order to include these variations, the absolute value of the deviation between the $\alpha = 0$ measurements for the same spatial configuration was added to the propagated, explicitly quantified uncertainty bounds of both $\alpha = 0$ and $\alpha = 4$ measurements to yield a final uncertainty estimate. Thus the error bars presented for the time-partial-space and time-full-space averaged mean flow profiles (Sec. 3.1) and the depth-averaged incoming streamwise flow to the elements (Sec. 3.5) represent both the explicitly and implicitly quantified uncertainties.

As the propagation of explicitly quantifiable uncertainties was more complicated for higher-order statistics and as the implicitly quantified experimental variations were dominant in the full error analyses, a reduced error analysis was applied to the higher-order statistics. Specifically, the sum of the statistical variations and the absolute value of the deviations between like measurements was taken as the uncertainty estimate for the following measurements: temporal and spatial turbulence spectra (Sec. 3.3), quadrant analysis of Reynolds stresses (also Sec. 3.3), and momentum flux profiles (Sec. 3.4).

3 Results

3.1 Existence of Developed Flow Within Array. In the present work, the classical definition (see, e.g., Ref. [15]) of "developed flow" is expanded somewhat to require both the mean streamwise flow and any mean vertical flow to be slowly varying with further streamwise distance into the array. In order to determine if the flows in the examined arrays reach the developed states, profiles of $|\bar{u}\rangle$, $|\bar{w}\rangle$ at the third and fourth measurement locations are shown overlaid in Fig. 3. The development of the

flow through the full length of the array may be found in the Supplemental material which is available under the "Supplemental Material" tab on the ASME Digital Collection.

For all stationary arrays (shown in light gray; red online), both streamwise and vertical flow profiles match within uncertainties at the two measurement locations. From this, it may be concluded that the flows are only slowly varying between the two measurement locations and thus both positions are taken to be within developed flow regions of the arrays.

Similarly, for the rotating (shown in dark gray; blue online) staggered RI and staggered RII arrays, both the streamwise and vertical flow profiles taken at the two measurement locations match within uncertainties and thus the third and fourth measurement locations are both taken to be within the developed flow regions.

The paired doublet and paired reverse doublet rotating arrays show a developed streamwise flow, but the vertical flow profiles differ between the two measurement locations. Therefore, the flows are not fully developed by the third measurement position and may or may not be developed by the fourth measurement position. Bearing this caveat in mind, in the remainder of the text, the flow in all arrays will be treated as developed at the fourth measurement position in the array.

Before leaving this section, it is important to note that the nonzero vertical flows exhibited in the time-partial-space profiles are confirmed in the time-full-space averaged profiles at the fourth measurement position, as shown in Fig. 4. The existence of a net spatially averaged vertical flow in a developed flow region of the array requires, by conservation of mass, transverse flow interactions between unit cells in the array and (presumably) the sides of the array. Thus, while the flow may be considered developed according to the definition presented, it may not be considered horizontally homogeneous.

3.2 Developed Flow, Mean 3D Flow Patterns. In Secs. 3.2.1–3.2.5, simplified sketches of the 3D mean flow patterns surrounding a small number of cylinders deep within the arrays are proposed. The patterns are based on $\bar{u}, \bar{w}$ collected in the transversely spaced sequence of vertical sheets at the fourth measurement position and $\bar{u}, \bar{v}$ collected in the intersecting vertically spaced horizontal sheets. Key features in the horizontal flow data are matched with the vertical flow data, bearing in mind local conservation of mass. The figures are presented in the Appendix in order to avoid inconvenient shifting of text and (the very large) figures. Finally, it is noted that the observed patterns are expected to depend on the height of the cylinders, but in the present work no exploration of this potential variation is conducted.

3.2.1 Stationary Cylinders. The proposed mean flow patterns around a stationary pair of cylinders are presented in Fig. 5,
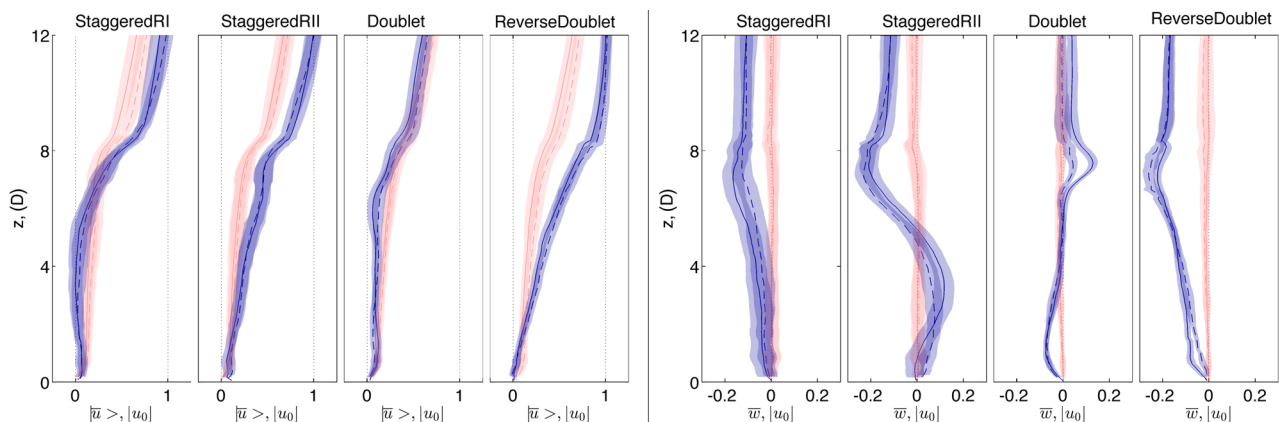

Fig. 3 Time-partial-space averaged streamwise (left group) and vertical (right group) flow profiles for each array at third (solid line) and fourth (dashed line) measurement positions. Light gray (red online) indicates $\alpha = 0$ and dark gray (blue online) indicates $\alpha = 4$. Uncertainties are shown by shaded region surrounding each line.
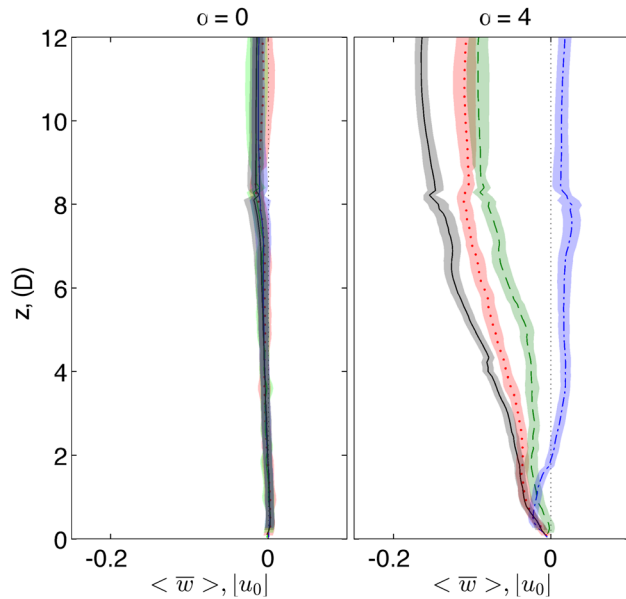
Fig. 4 Time-full-space averaged vertical flow profiles at the fourth measurement location of the arrays, spatial average taken over central unit cell. Dotted line (red online) indicates the staggered RI array, dashed line (green online) indicates the staggered RII array, dashed -dotted (blue online) line indicates the pair doublet array, and solid line (black) indicates the paired reverse doublet array.
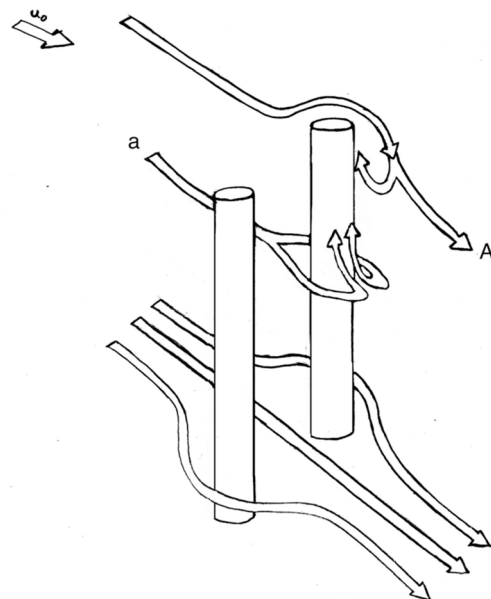

Fig. 5 Sketch of proposed "typical" mean flow patterns surrounding a stationary cylinder pair, deep within array. A and a are indications of the continuation of flow patterns from one unit cell in the array to the next.

including some indication of the flow between pairs of cylinders, from streamline A to streamline a. Figure 15 (given in the Appendix) presents and describes the supporting streamwise, transverse, and vertical flow data.

The key features of the streamwise flow patterns are increased flow between cylinders in a pair and flow reduction in the wake of each cylinder. The transverse flow diverges in front of the cylinders and converges behind them with some additional convergence behind the individual cylinders. The vertical flow shows that near the very top of the cylinder, there is upward flow in front and downward flow behind the cylinder. At lower heights within the array, however, this trend reverses with negative vertical flow on the front face of the cylinder and positive vertical flow on the rear face of the cylinder.

These features of the flow are in keeping with mean flow patterns previously reported by Stoesser et al. [18,20,21] for a finite-height array of cylinders and also with the wake-interaction behavior reported by Zdravkovich [22] and others (see Sumner [23]) for a closely spaced pair of cylinders.

3.2.2 Paired Doublet. The proposed mean flow patterns around a doublet-rotating pair of cylinders are presented in Fig. 6. Figure 16 (given in the Appendix) presents and describes the supporting streamwise, transverse, and vertical data.

Most notably, the streamwise flow reverses between cylinders in a pair. The transverse flow again diverges in front of and converges behind the pair. At the top of the array, the vertical flow shows upward and downward flown not only over the cylinders but also between them. These flow features suggest the existence of a virtual elliptical body, as described by Chan et al. [3] for isolated pairs of doublet-rotating cylinders. At lower heights within the array, there is upward flow and downward flow within the entrained boundary layer around the cylinders and, given the rotation of the cylinders, this suggests spiraling flow around the cylinders. The determining factor for whether the vertical flow around a cylinder is positive or negative is unclear, but could potentially be due to initial conditions or operating conditions (such as element wobble.) Once initiated, however, it is believed that the direction of the vertical flow is relatively stable. It was observed
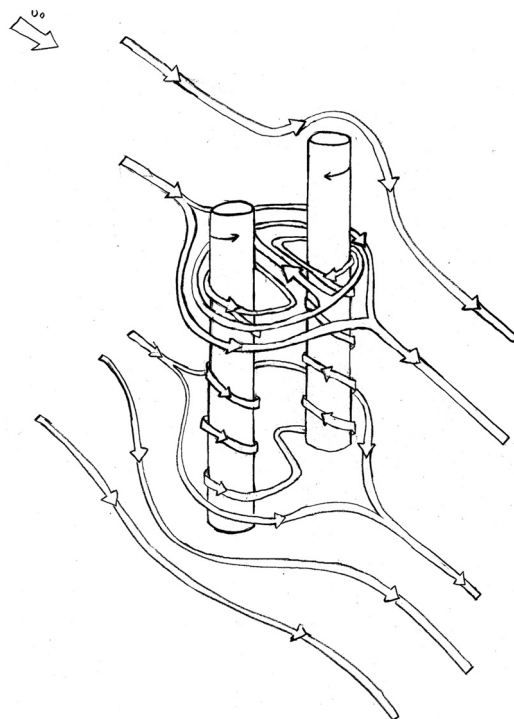
Fig. 6 Sketch of proposed typical mean flow patterns surrounding a paired doublet-rotating cylinder pair, deep within array

to be consistent between data sets taken sequentially at $\alpha = 2$ and $\alpha = 4$. As a rough estimate, therefore, taking an appropriate time scale to be the advective time scale $T = D/u_0$, the stability of the directional orientation was at least $O(10^4 T)$.

3.2.3 Paired Reverse Doublet. Figure 7 presents the hypothesized dominant flow pattern for a cylinder pair in the paired reverse doublet array, including some indication of the repetition

of the pattern from one cylinder pair to the next: A to a and B to b. Figure 17 presents and describes the supporting streamwise, transverse, and vertical flow data.

In the streamwise direction, the proposed flow patterns include a region of high streamwise flow between cylinders in a pair and reversal of streamwise flow to the outer sides of the cylinder pair. The transverse flow in this case converges in front of and diverges behind the pair. There is a strong vertical flow down into the array near the top of the array both at the cylinders and between them. In the far-wake of the cylinder pair, this downward flow persists to lower heights within the array. There is also a region of marginal upward flow near the top of the array in front of and to the sides of the pair and at lower heights in the array, upward flow occurs immediately behind cylinders and marginally to the sides of a pair.

3.2.4 Staggered RI. Figure 8 presents the hypothesized mean flow patterns around a subset of cylinders within the staggered RI array. Figure 18 (given in the Appendix) presents and describes the supporting streamwise, transverse, and vertical flow data.

Specifically, the proposed flow patterns include channels of positive and negative streamwise flows between columns of elements and channels of positive and negative transverse flows between rows of elements. A relatively uniform downward flow exists above the array, with regions of higher downward flow just behind the cylinders and at the downstream-moving edge of the cylinders. There is a slight upward flow near the cylinders at lower heights within the array.

3.2.5 Staggered RII. A simplified sketch of the hypothesized dominant flow patterns around a subset of cylinders in the staggered RII array is presented in Fig. 9. Figure 19 presents and describes the supporting streamwise, transverse, and vertical flow data.

It is possible to draw an analogy between alternating adjacent elements in the array and the paired doublet and reverse-doublet arrays: the cylinders marked A and B may be interpreted as a doublet-type rotating pair, while cylinders B and C may be interpreted as a reverse doublet-type rotating pair.

The proposed flow patterns include for the doublet-type pairs (A and B): channels of negative streamwise flows; divergent and convergent transverse flows upstream and downstream, respectively, of the "pairs"; and upward flow at the top of the array and downward flow within the array. For the reverse-doublet type pairs (B and C), the proposed flow patterns include: channels of positive streamwise flows; convergent and divergent transverse flows, in front of and behind, respectively, the pairs; and downward flow at the top of the array and upward flow within the array.

Fig. 8 Sketch of proposed typical mean flow patterns surrounding a subset of cylinders, deep within the staggered RI array

Fig. 9 Sketch of proposed typical mean flow patterns surrounding a subset of cylinders, deep within the staggered RII array. Cylinders A and B may be treated as a doublet-type rotating pair; cylinders B and C may be treated as a reverse-type rotating pair.

3.3 Turbulence Structure Within Array. Temporal and spatial power spectral densities of the system are examined in order to provide the details on the length and time scale of the individual turbulent structures in the system. (Note that the frozen turbulence assumption typically used to equate temporal and spatial spectra is not valid within an array, see e.g., Ref. [17].) The spatial spectra were taken along transverse and vertical lines running just behind the elements in row $176D$. The spectra were computed from each data realization and ensemble averaged. The resulting mean spectra are presented in Fig. 10. The temporal spectra were taken at each point in a $1D \times 1D$ region just downstream of an element or element pair and spatially averaged. This was repeated for the data collected at higher acquisition rates and the resulting partial spectra were combined to yield more complete spectra. These resulting spectra are presented in Fig. 11. All spectra have been normalized by their total power in order to allow clear comparison of the distribution of power; in general, the rotating arrays contain up to a factor of nine increase in the power over the stationary arrays.
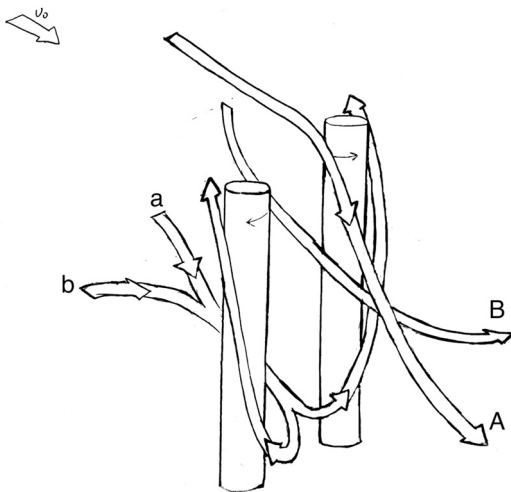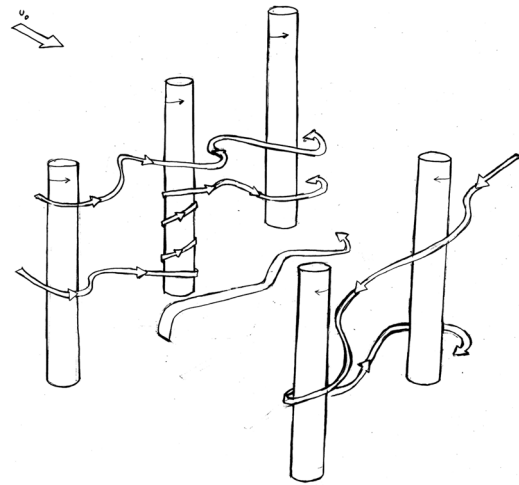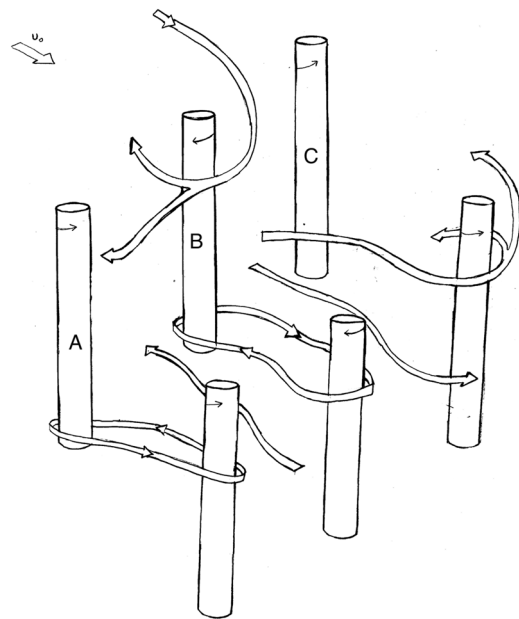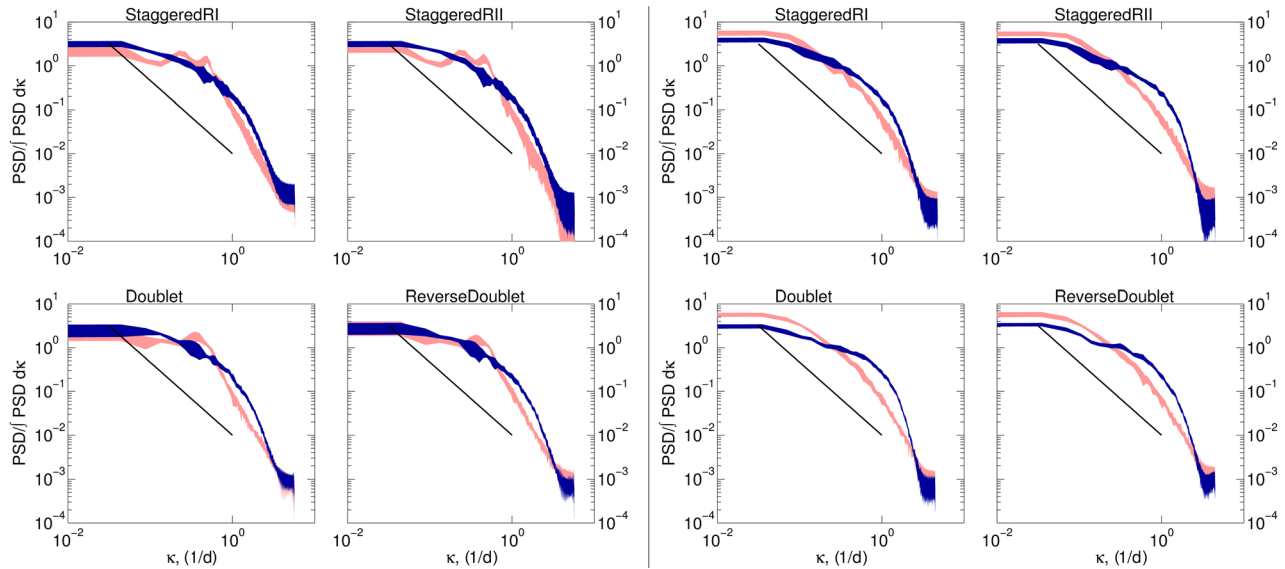

Fig. 7 Sketch of proposed typical mean flow patterns surrounding a paired reverse doublet-rotating cylinder pair, deep within array. A and a and B and b are indications of the continuation of flow patterns from one unit cell in the array to the next.

Fig. 10 Normalized spatial power spectral density of u'. Spectra taken over transverse (left group) or vertical (right group) lines of data just behind elements at $176D$ and ensemble averaged over each data realization. Light gray (red online) indicates a stationary array, dark gray (blue online) indicates a rotating array ($\alpha = 4$); the black line is $-5/3$ slope for reference. Thickness of lines indicates uncertainties.
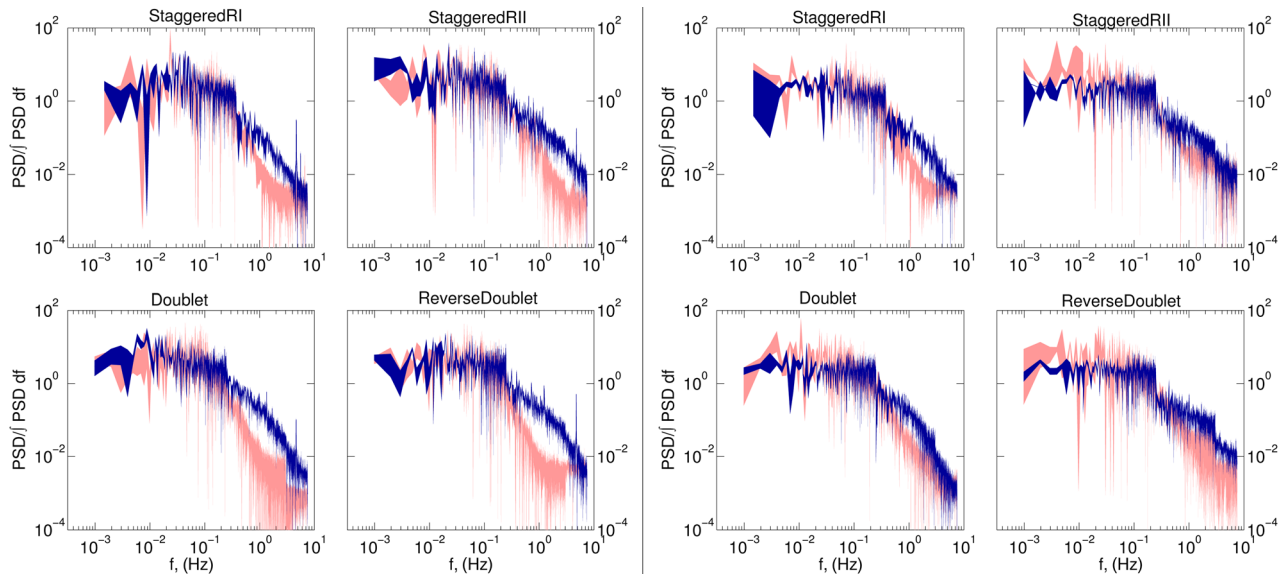

Fig. 11 Normalized temporal power spectral density of v' (left group) and w' (right group). Spectra taken at each point in small region within an element wake and spatially averaged. Light gray (red online) indicates a stationary array, dark gray (blue online) indicates a rotating array ($\alpha = 4$). Thickness of lines indicates uncertainties.

There are two notable features in the spatial spectra shown in Fig. 10. First, for the spectra taken in the horizontal plane (top box), at a scale of around half the diameter of the elements, there is a significant peak in the power distribution for the stationary array (light gray; red) which disappears for the rotating array (dark gray; blue). It is probable that the peak in the stationary array is associated with bluff-body vortex shedding of the cylinders and that this mode of vortex shedding is suppressed when the cylinders are rotating. A vorticity-based analysis of this is provided in the Supplemental material which is available under the "Supplemental Material" tab on the ASME Digital Collection. The second notable feature of the spatial power distribution spectra (which is observed in both the horizontal (left group) and vertical plane (right group)) is a shift from larger spatial scales to smaller spatial scales with the introduction of rotation.

The temporal spectra (Fig. 11) also show a shift in power distribution, in this case from low frequency structures to high frequency structures. Again, this shift is observed in the spectra of both transverse velocity fluctuations (left group) and vertical velocity fluctuations (right group), thus indicating no significant directional anisotropy.

Combining the information from the spatial and temporal spectra, there is indication that the turbulent power in the arrays shifts from slow, spatially larger, higher magnitude turbulent events to fast, spatially smaller, lower magnitude turbulent events with the introduction of element rotation.

In order to further educe the turbulent structure, particularly in the context of momentum exchange between the flow within the array and the flow above the array, a quadrant-based decomposition of the Reynolds shear stress, $u'w'$, is considered. The four quadrants are defined and denoted as Q1: $u' > 0, w' > 0$; Q2: $u' < 0, w' > 0$; Q3: $u' < 0, w' < 0$; and Q4: $u' > 0, w' < 0$. Conceptually, a Q2 (ejection) event brings locally lower momentum

fluid upward, while a Q4 (sweep) event brings locally higher momentum fluid downward. A Q1 (outward interaction) event brings locally higher momentum fluid upward and a Q3 (inward interaction) event brings locally lower momentum fluid downward. Thus, Q2 and Q4 events contribute positively to a higher momentum within the array. For a stationary array, the typical paradigm is for fluid momentum to increase with the increasing height, with a sharp increase just above the array, so it is typically more common for a downward perturbation to bring a locally higher momentum (Q4) rather than a locally lower momentum (Q3) and an upward perturbation to bring a locally lower momentum (Q2) rather than a locally higher momentum (Q1).

The equations describing the quadrant hole decomposition are as follows (based largely on Ref. [24], but making minor adaptations to accommodate non-negligible Q1 and Q3 events):

$$H = \frac{|\overline{u'w'}_{\text{threshold}}|}{|\overline{u'w'}|} \tag{1}$$

$$I_{i,H,t}(u',w',t) = \begin{cases} 1 & (u'w') \in i, |u'w'| \geq H|\overline{u'w'}| \\ 0 & \text{otherwise} \end{cases} \tag{2}$$

$$S = \frac{1}{T}\sum_t |u'(x,z,t)w'(x,z,t)|dt \tag{3}$$

$$S_{i,H} = \frac{1}{T}\sum_t |u'(x,z,t)w'(x,z,t)|I_{i,H,t}(x,z,t)dt \tag{4}$$

$$S^f_{i,H} = \frac{S_{i,H}}{S} \tag{5}$$

$$D^f_{i,H} = \frac{1}{T}\sum_t I_{i,H,t}dt \tag{6}$$

where H represents the hole size (i.e., minimum size threshold), I represents the conditional sampling function, S represents the mean Reynolds shear stress, and $S_{i,H}$ represents a Reynolds shear stress event in quadrant i at hole size H. $S^f_{i,H}$ represents the quadrant stress fraction—the fraction of the total stress at a given point in space which is contributed by event type i, above a certain threshold stress level H. $D^f_{i,H}$ represents the quadrant duration fraction—the fraction of the total measurement time for which a point in space is experiencing an event of type i, above a certain threshold stress level H.

Considering first the stationary array (shown in light gray; red). The spatially averaged duration fraction profiles (left, Fig. 12) show that Q2 events (solid line) occur most frequently within the array with Q4 events (dashed line) of secondary importance. Farther above the array, Q2 and Q4 events occur with roughly the same frequency. The spatially averaged stress fractions (right, Fig. 12) show that Q4 events (dashed line) contribute the most

strongly within the array and with Q2 events (solid line) of secondary importance. Again, above the array, Q2 and Q4 events contribute roughly equally to the stress. Restated in more physical terms, at the critical junction at the height of the array, the Q4 (sweep) events bringing high momentum fluid down into the array occur less frequently than the Q2 (ejection) events bringing low momentum fluid up out of the array, but while relatively infrequent, the Q4 events are much stronger that the Q2 events and therefore may be said to dominate the momentum exchange between the within array flow and above array flow.

With the introduction of rotation (shown in dark gray; blue), the spatially averaged duration fraction profiles (left, Fig. 12) show a significant drop in frequency of Q2 events, across the entire measurement height. This is seen for all arrays, with the one exception of the doublet array where above $z = 10D$, the frequency of Q2 events recovers to levels observed for the stationary array. Within the arrays, the decrease in Q2 duration fraction corresponds to increases in Q1 (dashed–dotted line) and Q3 (dotted line) duration fractions while the Q4 fractions remain comparable to the stationary case. In the staggered RII and doublet case, the comparability of the Q4 fraction persists above the array, but for the staggered RI and the reverse doublet there is a peak in Q4 at the height of the array which is larger than for the stationary case.

The spatially averaged stress fractions (right, Fig. 12) show that with the introduction of rotation the Q4 fraction drops significantly across the entire height of the array, again excepting only above the doublet array. Also as before, within all arrays the contributions to the stress from the Q1 (dashed–dotted line) and Q3 (dotted line) quadrants increase while the Q2 contribution remains comparable. Above the arrays, there is variation in Q2 stress fraction behavior between arrays: for the staggered RII array, the Q2 stress fraction remains comparable to the stationary case; for the doublet array, the Q2 stress fraction above the doublet array shows a drop; and for both the staggered RI and reverse doublet, the Q2 stress fraction peaks near the top of the canopy before falling again to levels comparable to the stationary arrays.

To restate these trends in more physically comprehensible terms, for the staggered RI, staggered RII, and reverse doublet arrays, the drop in Q2 event duration while maintaining relative comparability in stress fraction indicates that ejections have become fewer, but stronger, particularly in the region near the top of the staggered RI and reverse doublet arrays. The relative comparability of Q4 event duration and drop in stress fraction indicate that the sweep events have become generally weaker. Thus, while there are more sweep events above the array and in the top quarter of the array, the ejection events dominate the momentum transfer in these regions. Lower within the array, events of all types occur almost equally frequently and contribute almost equally to the momentum transfer.

3.4 Momentum Transport Into Array. The time–space averaged momentum equation is given as follows, assuming that
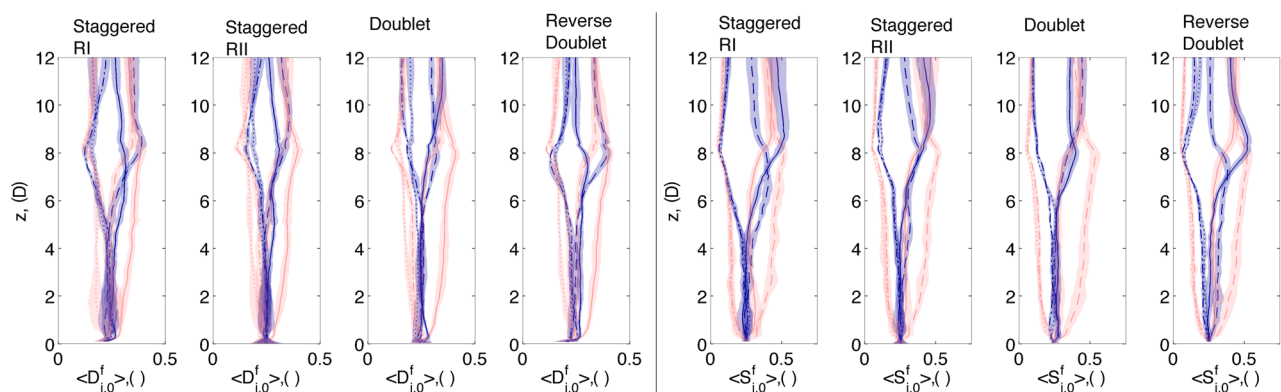

Fig. 12 Spatially averaged duration fraction (left) and stress fraction (right) of $u'w'$ events in quadrant 1 (−·), quadrant 2 (−), quadrant 3 (··) and quadrant 4 (− −). (Hole size = 0). $\alpha = 0$ in light gray (red online), $\alpha = 4$ in dark gray (blue online).

there are no body forces on the system, the element density of the array is uniform in space and time, and the elements are rigid

$$0 = -\frac{\partial \langle \overline{u_i} \rangle}{\partial t} - \frac{1}{\rho} \frac{\partial \langle \overline{p} \rangle}{\partial x_i} - \frac{\partial}{\partial x_j} \left(\langle \overline{u_j} \rangle \langle \overline{u_i} \rangle + \langle \overline{u_i' u_j'} \rangle + \langle \tilde{\overline{u}}_i \tilde{\overline{u}}_j \rangle \right) + f_i$$

(7)

where f_i in the last term includes viscous dissipation, form drag per unit fluid volume, and viscous drag per unit fluid volume and is not determinable from the given experiments. Based on the previously determined characteristics of the array, it is further assumed that the system is steady-state and that the flow is developed in the streamwise direction by the fourth measurement position in the array (i.e., $\partial (\cdot)/\partial x = 0$).

Concentrating on the streamwise momentum balance, a full comparison of the remaining terms (not including f_x) is provided in the Supplemental material which is available under the "Supplemental Material" tab on the ASME Digital Collection. It was concluded that the terms associated with transverse flows are typically smaller than the terms associated with the vertical flows, but non-negligible. In the present work, however, as the interaction between the flow within the array and flow above the array is of primary interest, here only the integral form of the vertical correlation terms will be considered for clarity.

Figure 13 presents the fluxes of streamwise momentum due to vertical flows, separating contributions from mean flows (solid lines), Reynolds stresses (dashed lines), and dispersive stresses

(dotted lines). For the stationary arrays (shown in light gray; red), only Reynolds stress-driven fluxes are significant, as would be expected from previous literature.

For the staggered RI, staggered RII, and reverse doublet arrays, the Reynolds stress flux at the top of the arrays ($z = 8D$, controlling the momentum exchange between above the array and within the array) increases sharply (up to a factor of 2.7) from the stationary to the rotating case. For the staggered RI and staggered RII arrays, the Reynolds stress flux at the top of the array is comparable to the mean flux, while at the top of the reverse doublet array, the mean flux is a factor of 2.3 higher than the Reynolds stress flux. For these three arrays, the dispersive stress flux at the top of the array is negligible in comparison to the other fluxes. However, in the staggered RII array, the dispersive stress flux contributes significantly to the redistribution of the momentum throughout the height of the array.

The doublet array, in contrast with other arrays, interacts relatively less with the flow above the array, which is not surprising considering the analogy of the rotating doublet array with a stationary array of larger elements, via the formation of virtual elliptical bodies around the pairs. What interaction does exist, however, largely reverse the trends of the other arrays: the Reynolds stress still drives a flux into the top of the array, but the mean flow and dispersive stress drive fluxes out the top of the array. All fluxes at the top of the array are of the same order of magnitude.

3.5 Quantifying Array Performance. Following Refs. [13,14], for a wind turbine array, the (cube of the) mean streamwise velocity spatially averaged over the frontal area of the turbine (a disk for HAWTs and a rectangle for VAWTs) may be taken as an indicator of the power resource available within the array. Adopting this metric (hereafter referred to as the "performance" of the array) allows a quantitative comparison between the drastically different flow patterns exhibited by the arrays.

In the present work, the mean incoming streamwise flow, $\langle \overline{u^3} \rangle|_{in}$, was computed from the horizontal sheet data as a partial-spatial average of $\overline{u^3}$ taken $1.25D$ upstream of the elements over the projected $1D$ transverse span of an element. This value was computed for each element in a repeating unit cell of the array and the average over all elements was taken as the value of $\langle \overline{u^3} \rangle|_{in}$ at that height in the array. A spline fit between the measurements at
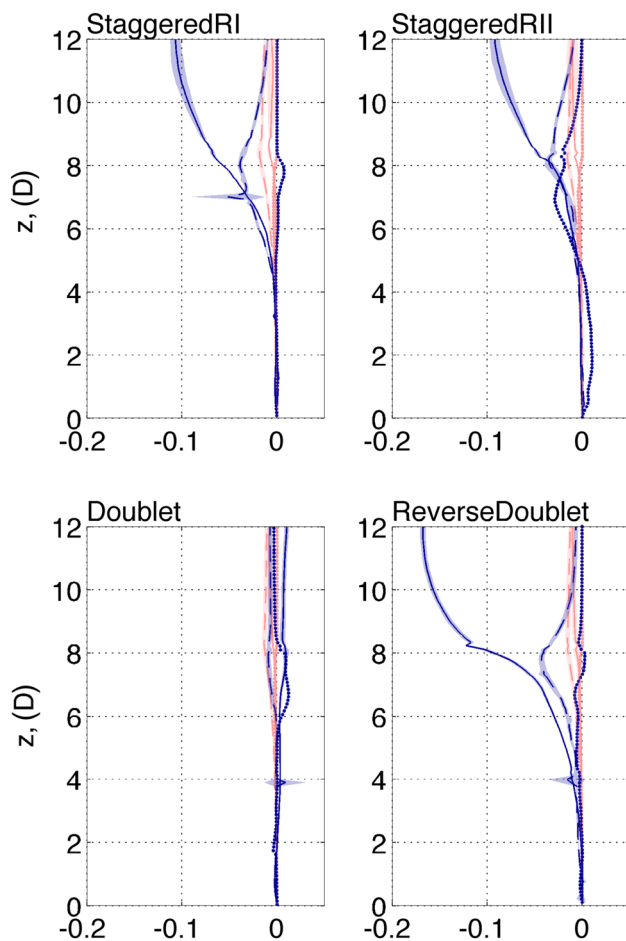

Fig. 13 Comparison of streamwise momentum fluxes: from mean flow, $\langle \overline{w} \rangle \langle \overline{u} \rangle$, (solid line); from Reynolds stresses, $\langle \overline{u'w'} \rangle$, (dashed line); and from dispersive stresses, $\langle \tilde{\overline{u}} \tilde{\overline{w}} \rangle$, (dotted line). Stationary array shown in light gray (red online), rotating array shown in dark gray (blue online).
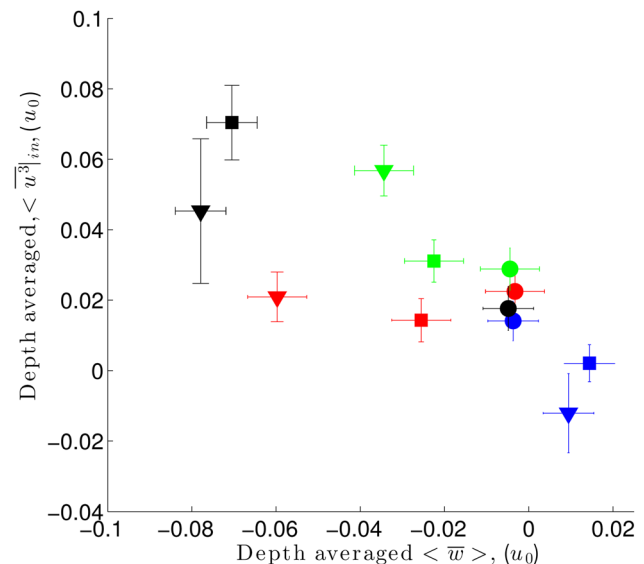

Fig. 14 The depth averaged mean incoming streamwise flow, $\langle \overline{u^3} \rangle|_{in}$, plotted against the depth-time-space averaged vertical flow. Medium gray (red online) indicates staggered RI array, light gray (green online) indicates staggered RII array, dark gray (blue online) indicates paired doublet array, and black indicates paired reverse doublet array. Circles indicate $\alpha = 0$, squares indicate $\alpha = 2$, and triangles indicate $\alpha = 4$.

the different heights and integration of the spline over the height of the array allowed a single depth averaged estimate to be obtained. The result is plotted against a depth-average of $\langle \overline{w} \rangle$ in Fig. 14.

Among the rotating arrays (square and triangle markers), the paired reverse doublet array (black) had the highest depth-averaged $\overline{|u^3|}_{in}$, reaching a factor of 4 improvement when compared to the corresponding stationary array. The staggered RII array (light gray; green) and staggered RI array (medium gray; red) had the second and third best performances (respectively), while the paired doublet array (dark gray; blue) had the lowest performance.

4 Discussion

Within the developed flow region of rotating-element arrays, it has been shown that regions of flow experiencing similar rotational influence from the elements are connected into patterns spanning multiple elements. It has also been shown that significant mean vertical flows exist within the array. As these local vertical flows are not generally balanced over a repeating unit cell of the array, it will result in net spatially averaged vertical flows. In turn, these require (by mass conservation) transverse flow interactions between unit cells in the array and (presumably) the sides of the array. Thus, the rotation of the elements in the array has the potential to both induce a net mean vertical inflow of high streamwise-momentum fluid from above the array and also divert and redistribute (favorably or unfavorably) the injected momentum within in the array.

The flow patterns in the paired reverse doublet array were found to be the most favorable in terms of maintaining high incoming streamwise flows to the elements. Particularly, strong vertical flows into the array were induced, while the relatively confined transverse flow patterns mixed the injected momentum, but did not strongly remove it from the array. Conversely, the staggered RI array, which also induced significant vertical flows into the array, exhibited very strong transverse channeling which diverted and removed the added momentum via the sides of the array, resulting in an exceptionally low performance. The paired doublet array behaved as an exact opposite to the staggered RI array: the transverse flow patterns were very spatially constrained and instead of a vertical inflow, there existed a net vertical outflow from the array. However, the paired doublet array performed even worse than the staggered RI array as the momentum resource within the array was not replenished from the flow above. Comparing these arrays, it is clear that two characteristics are required for an array to perform well: strong vertical inflow from above to replenish momentum within the array and spatially confined transverse flow patterns to ensure the momentum remains streamwise oriented instead of being diverted and lost transversely.

The temporal and spatial spectra of the flow fluctuations show almost an order of magnitude increase in the total turbulent power from the stationary case to the rotating case. The distribution of the power, however, shifts from slow, spatially large, higher-magnitude turbulent events to fast, spatially smaller, lower-magnitude turbulent events. Practically, this shift could have significant impact on the survival and fatigue lifetime of a turbine located within an array and highlights the need to consider the array-induced operating environment in the design of the turbines.

A rise in duration fraction and stress fraction of Q1 and Q3 events within the array suggests that the turbulence becomes less organized with the introduction of rotation, although at the height of the array ejection and sweep events still dominate. Cumulatively, the Reynolds stress-driven flux of streamwise momentum into the array from above is typically comparable to the mean-driven flux of momentum. The dispersive stress-driven flux is comparatively negligible in this regard. Combined, the total flux of streamwise momentum through the top of the array can increase by up to a factor of 5.7 between the stationary and rotating cases.

The patterns of flow within the array were insensitive to the rotation rate of the elements. However, the strengths of the patterns and the spatial extents of the patterns increased with increasing rotation rate and this generally induced larger vertical flow magnitudes.

5 Conclusions and Future Work

The key result of the present work is that the geometric and rotational configuration of the elements in an array may be tailored to maximize the streamwise flux through the array, with a $4\times$ improvement over a stationary array already demonstrated. The improved performance has been linked to net vertical mean flows into the array. This is in contrast to previously studied wind turbine arrays in which there was no net vertical mean flow and the critical vertical flux of streamwise momentum occurred via the turbulence-driven fluxes. While a net vertical mean flow does eliminate horizontal homogeneity and thus requires optimization of the full array simultaneously, it nevertheless provides another, potentially independent, means by which the flux of high momentum fluid into the array may be achieved.

The relative simplicity of the horizontal mean flow patterns within the arrays, which in turn determine the flow features critical to array performance, invites the development of a simple numerical model for the arrays. Such a model could be used to optimize an array over configurations not achievable experimentally or at least guide the selection of array configurations for a more detailed experimental analysis.

It is expected that the observed mean flow patterns have at least some dependence on the height of the cylinders. Motivated by this and the importance of the vertical inflows, it is noted that arrays with elements of heterogeneous heights may also be of interest as a potential means by which to further increase vertical mixing in the array.

Finally, as noted before, this work is not directly analogous to VAWT arrays and it would certainly be worthwhile to investigate the developed flow dynamics of arrays which improve upon some of the simplifications made in the present work. For example, within the same general experimental concept, it would be appropriate to reduce the rotation tip speed ratio elements by increasing the mean incoming freestream velocity (ideally to the point of operating in what would be a lift-based regime of element rotation, see Ref. [25]) and it would be vital to reduce the solidity of the elements [26]. A slightly more advanced, but nonetheless worthwhile correction would be to adjust the absolute rotation rate of the elements throughout the array in order to roughly maintain the same tip speed ratios based on local incoming flow speeds.

Appendix

The following notation will be used to denote flow features of interest: 1a, region of higher streamwise flow; 1b, region of reduced or reversed streamwise flow; 2a, region on convergent transverse flow; 2b, region of divergent transverse flow; 3a, region of positive vertical velocity, and 3b, region of negative vertical velocity. All other features of interest will be called out with higher numbers. Note that not all instances of a feature in the flow are called out in all pertinent panels, however, where the extension of a feature to other panels is not immediately obvious, the figure caption describes the spatial range of the feature.
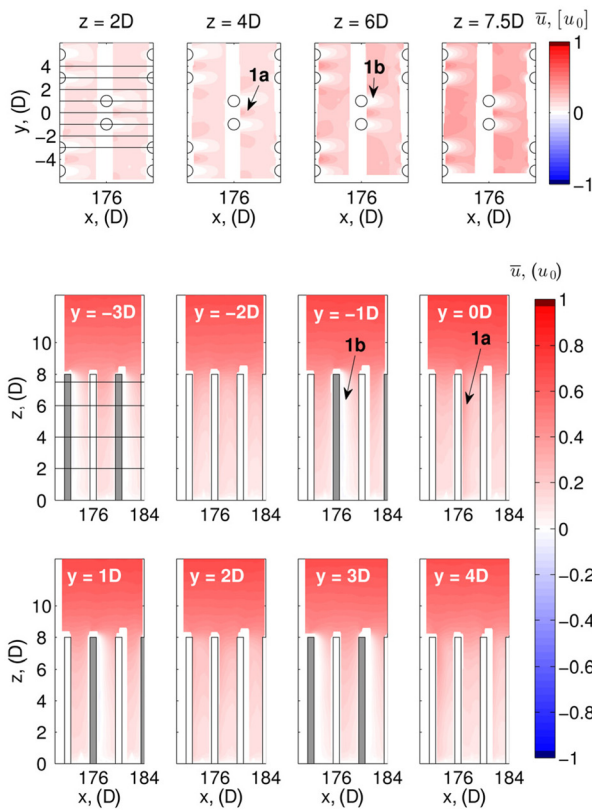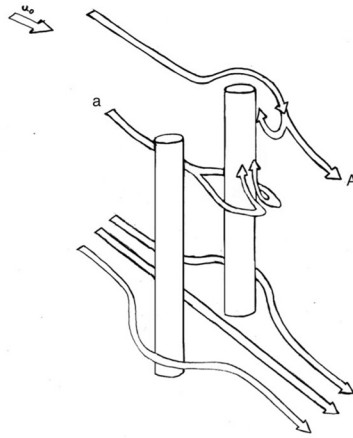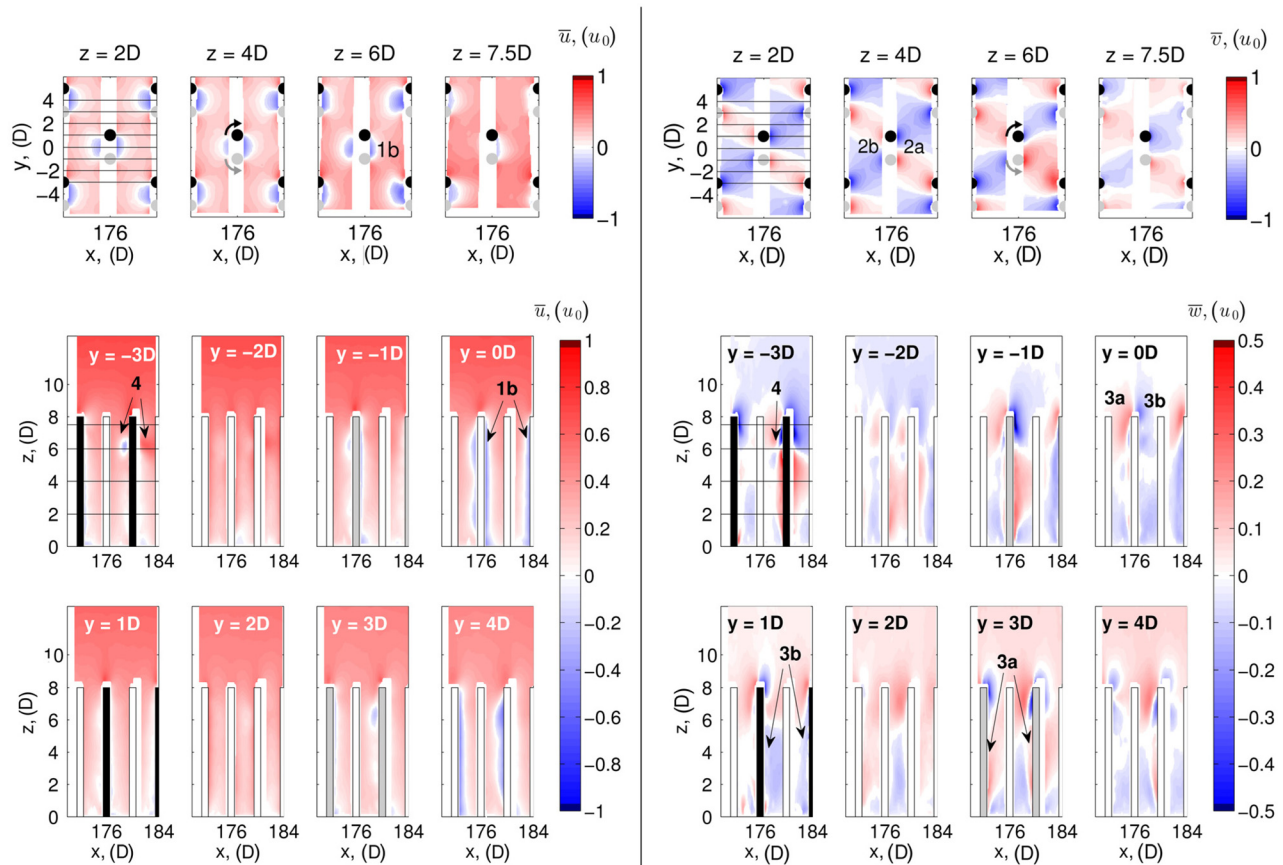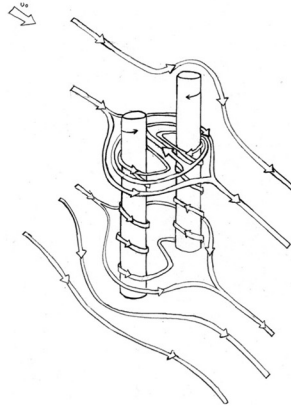
(a) Panels $z=4D$ and $y=0D$: 1a—higher streamwise flow between cylinders in pair. Panels $z=6D$ and $y=-1D$: 1b—lower or reversed streamwise flow in wakes of each individual cylinder.
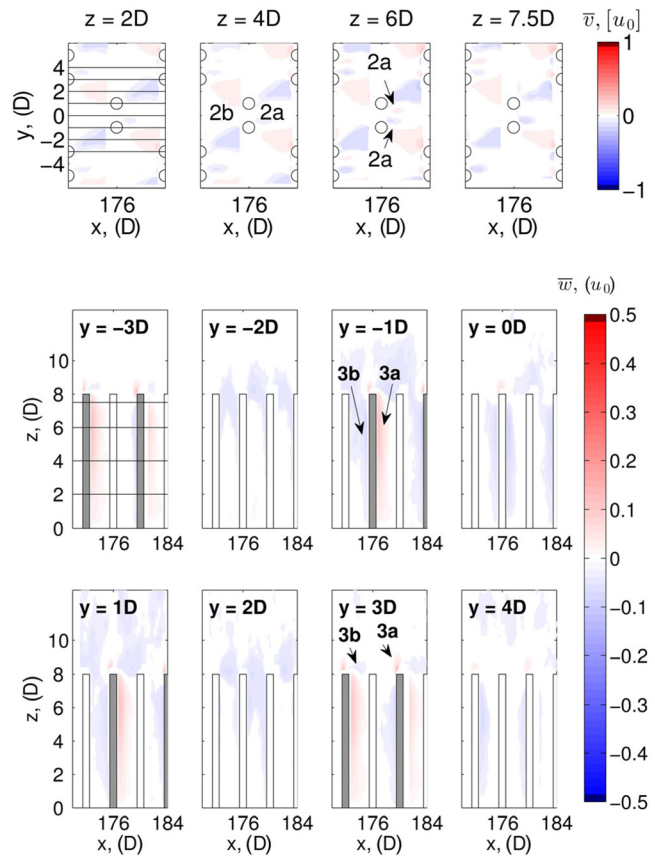
(b) Panel $z=4D$: 2a—transverse flow convergence behind the pair of cylinders, 2b—transverse flow divergence in front of the pair of cylinders. Panel $z=6D$: 2a—additional transverse flow convergence behind individual cylinders. Panel $y=-1D$: at lower heights within array, 3a—positive vertical flow behind cylinder and 3b—negative vertical flow in front of cylinder. Panel $y=3D$: near top of cylinder, 3a—positive vertical flow in front of cylinder and 3b—negative vertical flow behind cylinder.

Fig. 15 (a) $\overline{u}$ and (b) $\overline{v}$ and $\overline{w}$ in the paired geometry array for $\alpha = 0$. The synthesized sketch of flow patterns given in Fig. 5 is included at the top for convenient comparison. Black lines in the first panels mark locations of intersection with perpendicular sheets. In the horizontal sheets, (top row) open circles indicate the locations of the (stationary) cylinders. In the vertical sheets, dark gray rectangles indicate the data sheet intersected a (stationary) cylinder, while open rectangles indicate the locations of the cylinder rows, but the data sheet did not intersect a cylinder.

(a) Panels $z = 6D$ and $y = 0D$: 1b—region of reversed streamwise flow between cylinders in a pair. Panel $y = -3D$: 4—indicator of vortex dipole, which is discussed thoroughly in the Supplemental material which is available under the "Supplemental Material" tab on the ASME Digital Collection.

(b) Panel $z = 4D$: 2a—transverse flow convergence behind cylinder pair, 2b—transverse flow divergence in front of cylinder pair. Panel $y = 0D$: at top of array, 3a—positive vertical flow in front of cylinder and 3b—negative vertical flow behind cylinder. Panel $y = 1D$ and $y = 3D$: lower within array, there is either 3b—negative vertical flow or 3a—positive vertical flow surrounding the cylinders. Panel $y = -3D$: 4—indicator of vortex dipole, which is discussed thoroughly in the Supplemental material which is available under the "Supplemental Material" tab on the ASME Digital Collection.
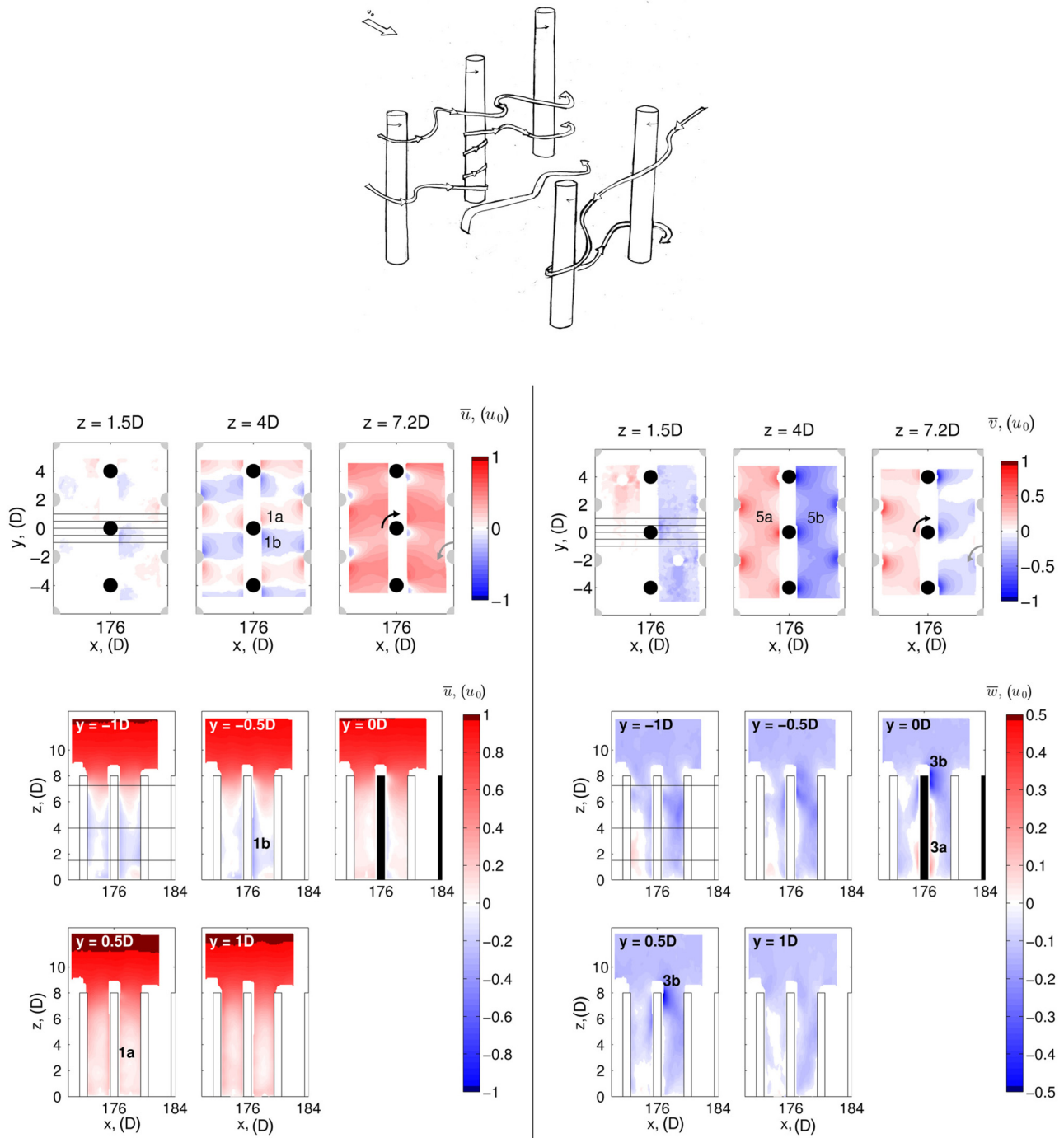
Fig. 16 (a) $\overline{u}$ and (b) $\overline{v}$ and $\overline{w}$ in the paired doublet array for $\alpha = 4$. The synthesized sketch of flow patterns given in Fig. 6 is included at the top for convenient comparison. Black lines in the first panels mark locations of intersection with perpendicular sheets. Black circles and rectangles indicate data sheet intersection with a clockwise rotating cylinder, gray circles and squares indicate data sheet intersection with a counterclockwise rotating cylinder, and open rectangles indicate the locations of the cylinder rows, but the data sheet did not intersect a cylinder.
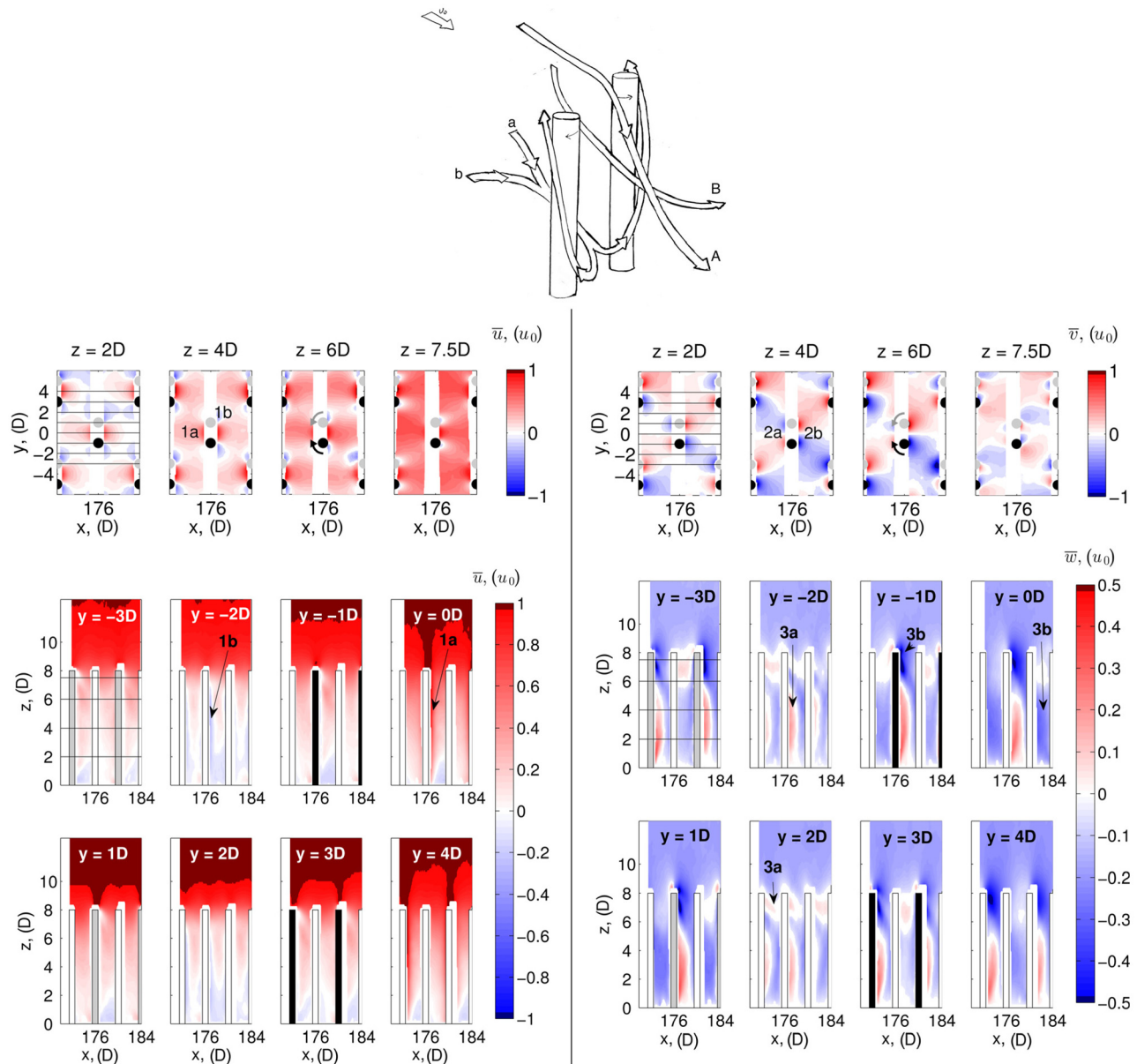
(a) Panels $z=4D$ and $y=0D$: 1a—increased streamwise flow between cylinders in a pair. Panels $z=4D$ and $y=-2D$: 1b—reversed streamwise flow to the sides of the cylinder pair.

(b) Panel $z=4D$: 2a—transverse convergence in front of cylinder pair and 2b—transverse divergence behind cylinder pair. Panel $y=2D$: at the top of the array, there is 3a—positive vertical flow in front of cylinders and to the sides of cylinder pair. Panel $y=-1D$: at top of array, 3b—negative vertical flow behind cylinders and between cylinders in pair. Panel $y=-2D$: lower within array, 3a—positive vertical flow to the sides of the cylinders and in near-downstream of the cylinders. Panel $y=0D$: lower within array, 3b—negative vertical flow in far downstream of cylinders or equivalently in front of next row of cylinders.

Fig. 17 (*a*) $\overline{u}$ and (*b*) $\overline{v}$ and $\overline{w}$ in the paired reverse doublet array for $\alpha=4$. The synthesized sketch of flow patterns given in Fig. 7 is included at the top for convenient comparison. For additional information, please see caption of Fig. 16.

(a) Panel $z = 4D$ and $y = 0.5D$: 1a—channel of positive streamwise flow between columns of cylinders. Panel $z = 4D$ and $y = -0.5D$: 1b—channel of negative streamwise flow between columns of cylinders.

(b) Panel $z = 4D$: 5a—channel of positive transverse flow between rows of elements and 5b—channel of negative transverse flow between rows of elements. Panels $y = 0D$ and $y = 0.5D$: at top of cylinder, 3b—negative vertical flow. Panel $y = 0D$: a—lower heights in array, 3a—positive vertical flow surrounding cylinder.

Fig. 18 (a) $\overline{u}$ and (b) $\overline{v}$ and $\overline{w}$ in the staggered RI array for $\alpha = 4$. The synthesized sketch of flow patterns given in Fig. 8 is included at the top for convenient comparison. For additional information, please see caption of Fig. 16.
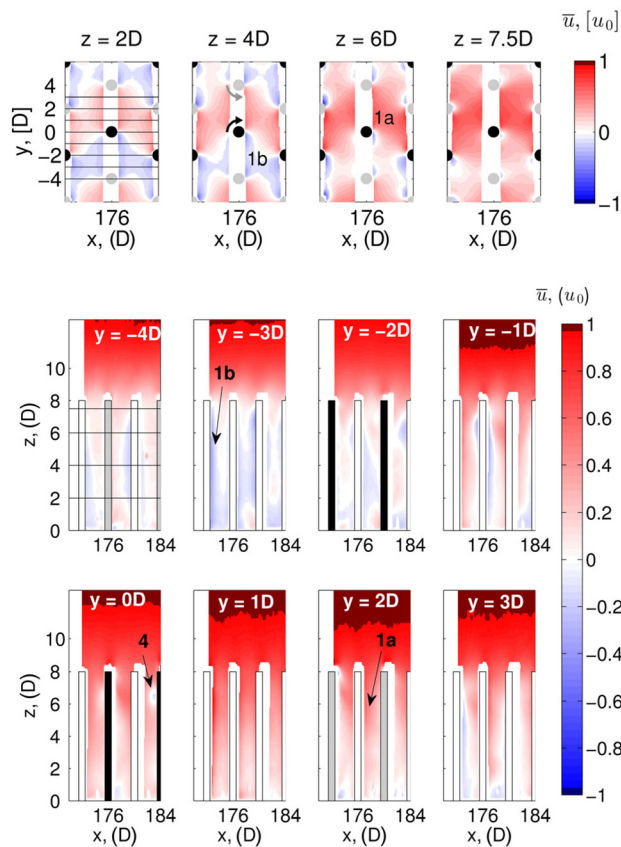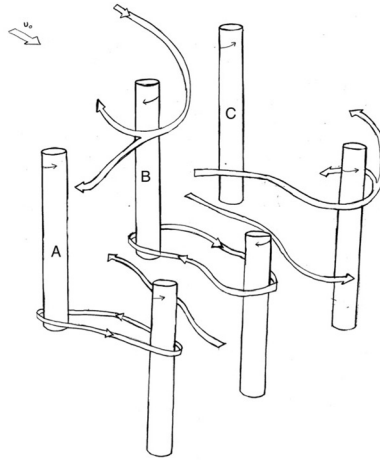
(*a*) Panels *z* = 6*D* and *y* = 2*D*: 1a—channel of increased streamwise flow between reverse doublet-type pair of cylinders. Panel *z* = 4*D* and *y* = −3*D*: 1b—channel of reverse streamwise flow between doublet-type pair of cylinders. Panel *y* = 0*D*: 4—indicator of vortex dipole, please see the Supplemental material which is available under the "Supplemental Material" tab on the ASME Digital Collection.
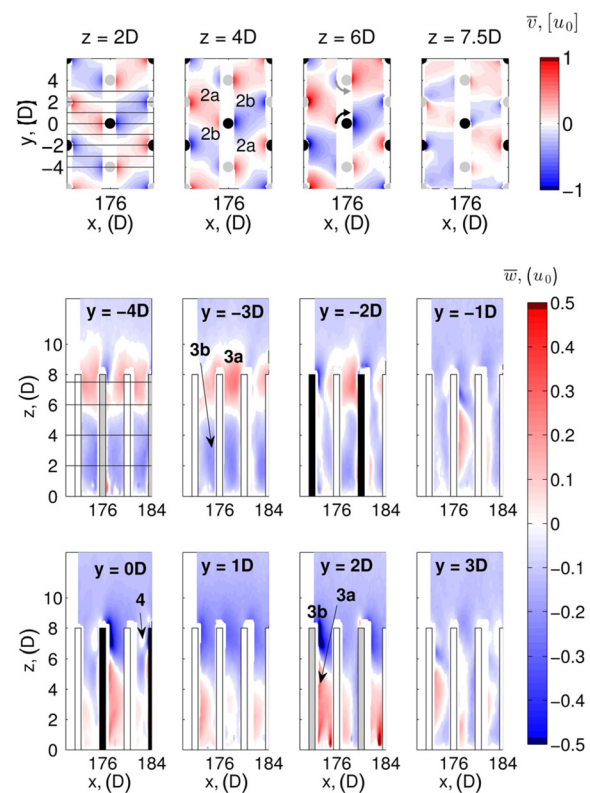
(*b*) Panel *z* = 4*D*: 2a—transverse flow convergence in front of reverse doublet-type pair of cylinders and behind doublet-type pair of cylinders; 2b—transverse flow divergence behind reverse doublet-type pair of cylinders and in front of doublet-type pair of cylinders. Panel *y* = −3*D*: between doublet-type pair of cylinders, near the top of the array there is 3a—positive vertical flow and at lower heights within the array there is 3b—negative vertical flow. Panel *y* = 2*D*: between reverse doublet-type pair of cylinders, near the top of the array there is 3b—negative vertical flow and at lower heights within the array there is 3a—positive vertical flow. Panel *y* = 0*D*: 4—indicator of vortex dipole, please see discussion in the Supplemental material which is available under the "Supplemental Material" tab on the ASME Digital Collection.

Fig. 19 (*a*) $\overline{u}$ and (*b*) $\overline{v}$ and $\overline{w}$ in the staggered RII array for $\alpha = 4$. The synthesized sketch of flow patterns given in Fig. 9 is included at the top for convenient comparison. For additional information, please see caption of Fig. 16.

References

[1] Navrose, Meena, J., and Mittal, S., 2015, "Three-Dimensional Flow Past a Rotating Cylinder," J. Fluid Mech., **766**, pp. 28–53.

[2] Rao, A., Radi, A., Leontini, J., Thompson, M. C., Sheridan, J., and Hourigan, K., 2015, "A Review of Rotating Cylinder Wake Transitions," J. Fluids Struct., **53**, pp. 2–14.

[3] Chan, A. S., Dewey, P. A., Jameson, A., Liang, C., and Smits, A. J., 2011, "Vortex Suppression and Drag Reduction in the Wake of Counter-Rotating Turbines," J. Fluid Mech., **679**, pp. 343–382.

[4] Guo, X., Lin, J., Tu, C., and Wang, H., 2009, "Flow Past Two Rotating Circular Cylinders in a Side-By-Side Arrangement," J. Hydrodyn., **21**(2), pp. 143–151.

[5] Kumar, S., Gonzalez, B., and Probst, O., 2011, "Flow Past Two Rotating Cylinders," Phys. Fluids, **23**(1), p. 014102.

[6] Ueda, Y., Kida, T., and Iguchi, M., 2013, "Steady Approach of Unsteady Low-Reynolds-Number Flow Past Two Rotating Circular Cylinders," J. Fluid Mech., **736**, pp. 414–443.

[7] Yoon, H. S., Kim, J. H., Chun, H. H., and Choi, H. J., 2007, "Laminar Flow Past Two Rotating Circular Cylinders in a Side-by-Side Arrangement," Phys. Fluids, **19**(12), p. 128103.

[8] Yoon, H. S., Chun, H. H., Kim, J. H., and Park, I. L. R., 2009, "Flow Characteristics of Two Rotating Side-by-Side Circular Cylinder," Comput. Fluids, **38**(2), pp. 466–474.

[9] Dabiri, J. O., 2011, "Potential Order-of-Magnitude Enhancement of Wind Farm Power Density Via Counter-Rotating Vertical-Axis Wind Turbine Arrays," J. Renewable Sustainable Energy, **3**(4), p. 043104.

[10] Whittlesey, R. W., Liska, S., and Dabiri, J. O., 2010, "Fish Schools as a Basis for Vertical Axis Wind Turbine Farm Design," Bioinspiration Biomimetics, **5**.

[11] Duraisamy, K., and Lakshminarayan, V., 2014, "Flow Physics and Performance of Vertical Axis Wind Turbine Arrays," AIAA Paper No. 2014-3139.

[12] Kinzel, M., Mulligan, Q., and Dabiri, J. O., 2012, "Energy Exchange in an Array of Vertical Axis Wind Turbines," J. Turbul., **13**(38), pp. 1–13.

[13] Cal, R. B., Lebron, J., Castillo, L., Kang, H. S., and Meneveau, C., 2010, "Experimental Study of the Horizontally Averaged Flow Structure in a Model Wind-Turbine Array Boundary Layer," J. Renewable Sustainable Energy, **2**(1), p. 013106.

[14] Calaf, M., Meneveau, C., and Meyers, J., 2010, "Large Eddy Simulation Study of Fully Developed Wind-Turbine Array Boundary Layers," Phys. Fluids, **22**(1), p. 015110.

[15] Belcher, S. E., Harman, I. N., and Finnigan, J. J., 2012, "Wind in the Willows: Flows in Forest Canopies in Complex Terrain," Annu. Rev. Fluid Mech., **44**(1), pp. 479–504.

[16] Chamorro, L. P., and Porte-Agel, F., 2011, "Turbulent Flow Inside and Above a Wind Farm: A Wind-Tunnel Study," Energies, **4**(12), pp. 1916–1936.

[17] Finnigan, J. J., 2000, "Turbulence in Plant Canopies," Annu. Rev. Fluid Mech., **32**(1), pp. 519–571.

[18] Stoesser, T., Palau-Salvador, G., Rodi, W., and Diplas, P., 2009, "Large Eddy Simulation of Turbulent Flow Through Submerged Vegetation," Transp. Porous Media, **78**(3), pp. 347–365.

[19] Nikora, V., Ballio, F., Coleman, S., and Pokrajac, D., 2013, "Spatially Averaged Flows Over Mobile Beds: Definitions, Averaging Theorems, and Conservation Equations," J. Hydraul. Eng., **139**(8), pp. 803–811.

[20] Nepf, H. M., and Koch, E. W., 1999, "Vertical Secondary Flows in Submersed Plant-Like Arrays," Limnol. Oceanogr., **44**(4), pp. 1072–1080.

[21] Poggi, D., and Katul, G. G., 2008, "The Effect of Canopy Roughness Density on the Constitutive Components of the Dispersive Stresses," Exp. Fluids, **45**(1), pp. 111–121.

[22] Zdravkovich, M. M., 1987, "The Effects of Interference Between Circular Cylinders in Cross Flow," J. Fluids Struct., **1**(2), pp. 239–261.

[23] Sumner, D., 2010, "Two Circular Cylinders in Cross-Flow: A Review," J. Fluids Struct., **26**(6), pp. 849–899.

[24] Yue, W., Meneveau, C., Parlange, M., Whu, W., van Hout, R., and Katz, J., 2007, "A Comparative Quadrant Analysis of Turbulence in a Plant Canopy," Water Resour. Res., **43**(5), p. W05422.

[25] Araya, D. B., and Dabiri, J. O., 2015, "A Comparison of Wake Measurements in Motor-Driven and Flow-Driven Turbine Experiments," Exp. Fluids, **56**, p. 150.

[26] Araya, D. B., Colonius, T., and Dabiri, J. O., 2016, "Transistion to Bluff Body Dynamics in the Wake of Vertical-Axis Wind Turbines," (submitted).